Is the Filinov integral conditioning technique useful in semiclassical initial value representation methods?

Michael Spanner
Department of Physics, University of Toronto, Toronto, Ontario M5S 1A7, Canada
Chemical Physics Theory Group, Department of Chemistry, and Center for Quantum Information and Quantum Control, University of Toronto, Toronto, Ontario M5S 3H6, Canada

Victor S. Batista[a] and Paul Brumer
Chemical Physics Theory Group, Department of Chemistry, and Center for Quantum Information and Quantum Control, University of Toronto, Toronto, Ontario M5S 3H6, Canada

(Received 2 November 2004; accepted 10 December 2004; published online 17 February 2005)

The utility of the Filinov integral conditioning technique, as implemented in semiclassical initial value representation (SC-IVR) methods, is analyzed for a number of regular and chaotic systems. For nonchaotic systems of low dimensionality, the Filinov technique is found to be quite ineffective at accelerating convergence of semiclassical calculations since, contrary to the conventional wisdom, the semiclassical integrands usually do not exhibit significant phase oscillations in regions of large integrand amplitude. In the case of chaotic dynamics, it is found that the regular component is accurately represented by the SC-IVR, even when using the Filinov integral conditioning technique, but that quantum manifestations of chaotic behavior was easily overdamped by the filtering technique. Finally, it is shown that the level of approximation introduced by the Filinov filter is, in general, comparable to the simpler *ad hoc* truncation procedure introduced by Kay [J. Chem. Phys. **101**, 2250 (1994)]. © *2005 American Institute of Physics*. [DOI: 10.1063/1.1854634]

I. INTRODUCTION

Understanding quantum mechanical processes in systems with many coupled degrees freedom is a subject of great interest. Unfortunately, a rigorous quantum treatment of molecular dynamics is often impossible due to the exponential increase of required computer storage space and computational workload with dimensionality. It is therefore essential to develop and implement approximate methods that are both reliable and computationally tractable, of which semiclassical methods[1] are most promising. In this paper, we explore the efficiency of the Herman–Kluk (HK) semiclassical (SC) initial value representation (IVR) method,[2–4] one of a general class of semiclassical propagators[5–7] with emphasis on the utility and accuracy of the Filinov integral conditioning technique.[8–11] Such techniques were introduced to speed up convergence in semiclassical computations, a vital need if such computations are to be generally useful.

The HK SC-IVR is currently the most popular semiclassical approach. Unfortunately, the HK SC-IVR approach remains quite inefficient when applied to a number of interesting cases, primarily due to poor Monte Carlo (MC) statistics in the integration over initial phase space conditions. This is usually attributed to the (complex valued) integrand that may become highly oscillatory, leading to phase cancellation problems.

The Filinov filter,[8–11] described in Sec. II C, provides a means of analytically integrating out the contribution of neighboring trajectories in highly oscillatory regions. The original idea was to incorporate such a filter directly into an optimized sampling function when evaluating the IVR integrals by importance sampling Monte Carlo techniques.[10,11] Unfortunately, it has proven difficult to use the Filinov filter in this manner. Rather, the Filinov filter has typically been implemented in SC-IVR calculations via an alternative approach, where the contributions of trajectories that originate in oscillatory regions are down-weighted. Obviously, such an approach does not avoid sampling highly oscillatory regions and is therefore not optimal in terms of computational effort. However, it does minimize undesirable effects caused by rapid phase oscillations. The Filinov filter used in this way has been effective in accelerating the convergence of semiclassical calculations[11–18] (albeit they still remain time consuming) and is becoming part of the standard semiclassical methodology. Surprisingly, a detailed study of the utility of the Filinov filter has yet to be undertaken. This is the main issue addressed in this paper.

Below, the utility of the Filinov filter is explored in a number of nonchaotic and chaotic systems. The nonchaotic models consist of a one-dimensional (1D) anharmonic oscillator, a 2D linear triatomic system with dissociative dynamics, and a 2D model of nonadiabatic ICN photodissociation dynamics. In all of these nonchaotic systems, the Filinov filter is found to be quite inefficient if strong overdamping of the results is to be avoided. We analyze the reasons for the observed lack of efficiency and show that the nonchaotic systems considered *do not* exhibit rapid phase oscillations in regions of large integrand amplitude, explaining the ineffectiveness of the Filinov filter. The chaotic examples studied consist of two 1D nonadiabatically coupled oscillators, the quartic oscillator, the Henon–Heiles system, and the photodissociation of 2D H_2O. In these systems, the Filinov filter is

[a]Present address: Department of Chemistry, Yale University, New Haven, CT 06520-8107.

seen to be capable of alleviating convergence problems arising from regions of large phase oscillations and exponentially large integrand amplitude. However, the converged Filinov filtered results show incorrect level spacing distributions in the chaotic domain, albeit correct behavior in the regular regime. Thus, the Filinov filter overdamps the dynamics.

The paper concludes with a comparison of the Filinov filter method and an alternate *ad hoc* method proposed by Kay.[19] It is argued that the two methods introduce an equivalent level of approximation when applied to the semiclassical integrals.

II. METHODOLOGY

A. Herman–Kluk SC-IVR

The HK SC-IVR[2,7,19] approximates the quantum propagator

$$K(\mathbf{x}',\mathbf{x},t) = \langle \mathbf{x}' | e^{-i\hat{H}t/\hbar} | \mathbf{x} \rangle \tag{1}$$

as

$$K^{\mathrm{sc}}(\mathbf{x}',\mathbf{x},t) = \left(\frac{1}{2\pi\hbar}\right)^N \int d\mathbf{p} \int d\mathbf{q} C_{\mathbf{pq}t} e^{iS_{\mathbf{pq}t}/\hbar} \langle \mathbf{x}' | \mathbf{p}_t \mathbf{q}_t \boldsymbol{\beta} \rangle \times \langle \mathbf{pq}\boldsymbol{\beta} | \mathbf{x} \rangle, \tag{2}$$

where N is the number of degrees of freedom, $(\mathbf{p},\mathbf{q})$ are the initial coordinates and momenta for classical trajectories $\mathbf{p}_t = \mathbf{p}_t(\mathbf{p},\mathbf{q})$ and $\mathbf{q}_t = \mathbf{q}_t(\mathbf{p},\mathbf{q})$ obtained by integrating Hamilton's equations to time t, and $S_{\mathbf{pq}t}$ is the classical action integrated along these classical trajectories, given by

$$S_{\mathbf{pq}t} = \int_0^t d\tau [\mathbf{p}_\tau \cdot \dot{\mathbf{q}}_\tau - H(\mathbf{p}_\tau, \mathbf{q}_\tau)]. \tag{3}$$

The states $|\mathbf{pq}\boldsymbol{\beta}\rangle$, introduced by Eq. (2), denote multidimensional Gaussian wave packets with average position $\mathbf{q} = (q_1, q_2, \ldots, q_N)$ and momentum $\mathbf{p} = (p_1, p_2, \ldots, p_N)$, that is,

$$|\mathbf{pq}\boldsymbol{\beta}\rangle = \prod_{k=1}^N |p_k q_k \beta_k\rangle, \tag{4}$$

where

$$\langle x_k | p_k q_k \beta_k \rangle = \left(\frac{2\beta_k}{\pi}\right)^{1/4} \exp\left[-\frac{\beta_k}{2}(x_k - q_k)^2 + i p_k (x_k - q_k)/\hbar \right]. \tag{5}$$

The prefactor $C_{\mathbf{pq}t}$ is defined by

$$C_{\mathbf{pq}t} = \left\{ \det\left[\frac{1}{2}\left(\frac{\partial q_{tk}}{\partial q_j} + \frac{\beta_j}{\beta_k}\frac{\partial p_{tk}}{\partial p_j} - 2i\hbar\beta_j \frac{\partial q_{tk}}{\partial p_j} - \frac{1}{2i\hbar\beta_k}\frac{\partial p_{tk}}{\partial q_j} \right) \right] \right\}^{1/2}. \tag{6}$$

where q_{tk}, p_{tk} denote the kth component of the propagated coordinate and momentum at time t. The square root in this equation is chosen such that $C_{\mathbf{pq}t}$ is a continuous function of t with $C_{\mathbf{pq}0} = 1$. The Gaussian width parameters β_k are essentially arbitrary, but in practice the HK SC-IVR calculations are seen to be optimized when the β_k are chosen such that the coordinate space representation of $|\mathbf{pq}\boldsymbol{\beta}\rangle$ is about the same size as the initial wave function $\Psi_0(\mathbf{q})$.[7]

The full HK SC-IVR wave function at time t can then be written as

$$\Psi^{\mathrm{sc}}(\mathbf{x}',t) = \left(\frac{1}{2\pi\hbar}\right)^N \int d\mathbf{p} \int d\mathbf{q} C_{\mathbf{pq}t} e^{iS_{\mathbf{pq}t}/\hbar} \langle \mathbf{x}' | \mathbf{p}_t \mathbf{q}_t \boldsymbol{\beta} \rangle \times \langle \mathbf{pq}\boldsymbol{\beta} | \Psi_0 \rangle. \tag{7}$$

This semiclassical integral is typically evaluated using Monte Carlo integration with a sampling function $|\langle \mathbf{pq}\boldsymbol{\beta} | \Psi_0 \rangle|$. When $|\Psi_0\rangle$ is itself a Gaussian wave packet, the $\langle \mathbf{pq}\boldsymbol{\beta} | \Psi_0 \rangle$ projection can be evaluated analytically. The necessary time-dependent factors in Eq. (7) are integrated numerically using the following differential equations:

$$\frac{dp_{ti}}{dt} = -\frac{\partial H}{\partial q_{ti}}, \quad \frac{dq_{ti}}{dt} = \frac{\partial H}{\partial p_{ti}}, \tag{8}$$

$$\frac{d}{dt}\left(\frac{\partial p_{ti}}{\partial z_j}\right) = -\sum_{k=1}^N \left(\frac{\partial^2 H}{\partial p_{tk}\partial q_{ti}}\frac{\partial p_{tk}}{\partial z_j} + \frac{\partial^2 H}{\partial q_{tk}\partial q_{ti}}\frac{\partial q_{tk}}{\partial z_j} \right), \tag{9}$$

$$\frac{d}{dt}\left(\frac{\partial q_{ti}}{\partial z_j}\right) = \sum_{k=1}^N \left(\frac{\partial^2 H}{\partial p_{tk}\partial p_{ti}}\frac{\partial p_{tk}}{\partial z_j} + \frac{\partial^2 H}{\partial q_{tk}\partial p_{ti}}\frac{\partial q_{tk}}{\partial z_j} \right), \tag{10}$$

where $z = p$ or q.

In addition to the wave function, we compute both the autocorrelation function $\chi(t)$ and the associated energy spectrum $I(E)$, defined as

$$\chi(t) = \langle \Psi_0 | \Psi(t) \rangle = \langle \Psi_0 | e^{-i\hat{H}t/\hbar} | \Psi_0 \rangle \tag{11}$$

and

$$I(E) = \frac{1}{2\pi\hbar}\int_0^\infty dt e^{iEt/\hbar}\chi(t). \tag{12}$$

B. Nonadiabatic HK SC-IVR

This semiclassical formalism can be extended to model nonadiabatic dynamics on multiple electronic surfaces.[20,21] First, a classical Hamiltonian that encompasses the multiple surface problem must be constructed. Such a Hamiltonian was developed by Meyer and Miller[22] and is written, for the case of two potential energy surfaces, as

$$H(\mathbf{R},\mathbf{P};\mathbf{x},\mathbf{p}) = \frac{\mathbf{P}^2}{2M} + H_{el}(\mathbf{R};\mathbf{x},\mathbf{p}), \tag{13}$$

where

$$H_{el}(\mathbf{R};\mathbf{x},\mathbf{p}) = \tfrac{1}{2}H_{1,1}(\mathbf{R})[p_1^2 + x_1^2 - 1] + \tfrac{1}{2}H_{2,2}(\mathbf{R})[p_2^2 + x_2^2 - 1] + H_{1,2}(\mathbf{R})[p_1 p_2 + x_1 x_2]. \tag{14}$$

Here x_k and p_k are the coordinates and momenta of coupled oscillators modeling the electronic degrees of freedom, $\mathbf{R}$ and $\mathbf{P}$ are the nuclear coordinates and momenta, and $H_{i,j}$ are the components of the electronic Hamiltonian matrix.

When this Hamiltonian dynamics is propagated through SC-IVR, the wave function $\phi(x_1,x_2) = \phi(x_1)\phi(x_2)$ corresponding to the electronic oscillators is given by harmonic

oscillator states of $H'=p^2/2+x^2/2$, with $|\phi^{(1)}\rangle=|1\rangle|0\rangle$ if the first electronic surface is excited and $|\phi^{(2)}\rangle=|0\rangle|1\rangle$ if the second surface is excited. The nuclear wave function on the mth electronic surface is calculated using HK SC-IVR as

$$\Psi(\mathbf{R},m,t)=\left(\frac{1}{2\pi\hbar}\right)^N\int d\mathbf{Q}_0 C_{\mathbf{Q}t}e^{iS_{\mathbf{Q}t}/\hbar}\langle\mathbf{R}|\mathbf{P}_t\mathbf{R}_t\boldsymbol{\beta}\rangle\langle\phi^{(m)}|\mathbf{p}_t\mathbf{x}_t\gamma\rangle \times\langle\mathbf{P}_0\mathbf{R}_0\boldsymbol{\beta}|\Phi_0\rangle\langle\mathbf{p}_0\mathbf{x}_0\gamma|\phi^{(n)}\rangle, \tag{15}$$

where $\mathbf{Q}=(\mathbf{R},\mathbf{P},\mathbf{x},\mathbf{p})$, $d\mathbf{Q}_0=d\mathbf{P}_0d\mathbf{R}_0d\mathbf{p}_0d\mathbf{x}_0$, $|\Phi_0\rangle$ is the nuclear wave function initially on the nth electronic surface, and γ is the Gaussian width parameter for the electronic degrees of freedom.

C. Filinov Filter

Written as Eqs. (7) and (15), the HK SC-IVR method is seen to constitute a phase space average over the initial conditions of classical trajectories. Since we are in the semiclassical regime, the integrands are expected to become a highly oscillatory function of the initial coordinates due to the complex exponential dependence on $e^{iS/\hbar}$, increasing when neighboring trajectories diverge and separate with time. Furthermore, since the prefactor C_{pqt} is a function of the coordinate derivatives with respect to the initial conditions, the amplitude of a particular trajectory can become larger as time progresses and the trajectory diverges from its neighboring trajectories. Because of this, C_{pqt} is expected to increase approximately algebraically with time for regular trajectories and exponentially for chaotic trajectories, while the integrand phase becomes more and more oscillatory. Introducing some preconditioning of the integrand or preaveraging of neighboring trajectories to minimize these adverse effects therefore seems desirable. The Filinov filter[8–11] is applied to semiclassical methods for this reason and proceeds as follows.

Consider a general complex integral written as

$$I=\int d\mathbf{r}A(\mathbf{r})e^{i\phi(\mathbf{r})}, \tag{16}$$

where $A(\mathbf{r})$ is the amplitude (i.e., a real-valued function.) To precondition this integral, one inserts unity in the form of a normalized Gaussian integral, $1=(C/\pi)^{N/2}\int d\mathbf{r}'e^{-C(\mathbf{r}-\mathbf{r}')^2}$, to give

$$I=(C/\pi)^{N/2}\int d\mathbf{r}\int d\mathbf{r}'A(\mathbf{r})e^{i\phi(\mathbf{r})}e^{-C(\mathbf{r}-\mathbf{r}')^2}. \tag{17}$$

Since the Gaussian is localized around $\mathbf{r}'$ for large values of C, the phase function $\phi(\mathbf{r})$ can be approximated by a linear expansion about $\mathbf{r}'$, $\phi(\mathbf{r})\approx\phi(\mathbf{r}')+\nabla\phi(\mathbf{r}')\cdot(\mathbf{r}-\mathbf{r}')$, to give

$$I=(C/\pi)^{N/2}\int d\mathbf{r}'A(\mathbf{r}')e^{i\phi(\mathbf{r}')}\int d\mathbf{r}e^{-C(\mathbf{r}-\mathbf{r}')^2+i\nabla\phi(\mathbf{r}')\cdot(\mathbf{r}-\mathbf{r}')}, \tag{18}$$

where $A(\mathbf{r})$ was approximated by $A(\mathbf{r}')$. This approximation to $A(\mathbf{r})$ is again justified since the Gaussian is localized about $\mathbf{r}'$. Evaluating the $\mathbf{r}$ integral leads to

$$I=\int d\mathbf{r}'A(\mathbf{r}')e^{i\phi(\mathbf{r}')-|\nabla\phi(\mathbf{r}')|^2/4C}. \tag{19}$$

Preaveraging of the neighboring integration points then occurs through the gradient term in the exponential, and the contribution to the integral is small when the phase of the integrand becomes highly oscillatory. The "strength" parameter C controls the extent of the preaveraging, and it is noted that as $C\to\infty$, the original integral [Eq. (16)] is recovered.

This procedure can be applied to the semiclassical integral for $|\Psi^{\mathrm{sc}}\rangle$ by simply incorporating the factor $e^{-|\nabla_0\phi|^2/4C}$ into the integrand, where $|\nabla_0\phi|^2$ is the magnitude squared of the phase gradient with respect to the initial conditions and can be calculated (for the adiabatic case) as

$$|\nabla_0\phi|^2=\sum_{i=1}^N\left[\left(\frac{\partial\phi}{\partial q_i}\right)^2+\left(\frac{\partial\phi}{\partial p_i}\right)^2\right], \tag{20}$$

where

$$\frac{\partial\phi}{\partial q_i}=\sum_{j=1}^N\left[\frac{\partial p_{tj}}{\partial q_i}(x_j'-q_{tj})\right]+\left[\frac{\beta_i(p_{1i}-p_i)}{\beta_i+\beta_{1i}}\right], \tag{21}$$

$$\frac{\partial\phi}{\partial p_i}=\sum_{j=1}^N\left[\frac{\partial p_{tj}}{\partial p_i}(x_j'-q_{tj})\right]-\left[\frac{\beta_{1i}(q_{1i}-q_i)}{\beta_i+\beta_{1i}}\right]. \tag{22}$$

An analogous expression that includes both nuclear and electronic coordinates applies to the nonadiabatic case. Here $\hbar$ is set to 1 for ease of notation and the contribution to the phase of the semiclassical prefactor C_{pqt} is neglected. The latter is a standard approximation used when applying the Filinov filter to semiclassical integrals, simply because this phase cannot be easily included. Here the initial state $|\Psi_0\rangle$ was assumed to be the Gaussian state $|\mathbf{p}_1\mathbf{q}_1\boldsymbol{\beta}_1\rangle$. In calculating the semiclassical autocorrelation function $\chi^{\mathrm{sc}}(t)=\langle\Psi_0|\Psi^{\mathrm{sc}}(t)\rangle$, the phase derivatives are given by

$$\frac{\partial\phi}{\partial q_i}=\sum_{j=1}^N\left\{\frac{\partial q_{tj}}{\partial q_i}\left[\frac{\beta_j(p_{tj}-p_{1j})}{\beta_j+\beta_{1j}}\right]-\frac{\partial p_{tj}}{\partial q_i}\left[\frac{\beta_{1j}(q_{tj}-q_{1j})}{\beta_j+\beta_{1j}}\right]\right\}+\left[\frac{\beta_j(p_{1j}-p_j)}{\beta_j+\beta_{1j}}\right], \tag{23}$$

$$\frac{\partial\phi}{\partial p_i}=\sum_{j=1}^N\left\{\frac{\partial q_{tj}}{\partial p_i}\left[\frac{\beta_j(p_{tj}-p_{1j})}{\beta_j+\beta_{1j}}\right]-\frac{\partial p_{tj}}{\partial p_i}\left[\frac{\beta_{1j}(q_{tj}-q_{1j})}{\beta_j+\beta_{1j}}\right]\right\}-\left[\frac{\beta_{1j}(q_{1j}-q_j)}{\beta_j+\beta_{1j}}\right]. \tag{24}$$

This version of the Filinov filter as applied to SC-IVR is one of the simplest offered in the literature.[1,10,15,18,23] Section V discusses alternate versions that rely on keeping higher order terms when expanding in a Taylor series, or on more complicated representations of unity. The results reported in that section, however, suggest that these more advanced versions are essentially no better than the simpler version presented here.

III. NONCHAOTIC SYSTEMS

Although the Filinov filter has been used primarily in the literature for chaotic systems, it is instructive to first consider its utility in the nonchaotic regime. Consider a 1D anharmonic oscillator, initially used by Kay,[7] which is the sum of a Morse and harmonic potential defined by the Hamiltonian

$$H = -\frac{1}{2}p^2 + \frac{\epsilon}{2b^2}(1-e^{-bx})^2 + (1-\epsilon)\frac{1}{2}x^2, \tag{25}$$

where $\epsilon = 0.975$ and $b = 1/\sqrt{12}$. This particular anharmonic system poses no great numerical difficulties. The number of trajectories needed for convergence of up to six oscillations of a wave packet launched in the potential was 6400,[7] without the use of the Filinov filter. The system is included in the present study because the low dimensionality provides the opportunity to fully map and visualize the integrand of the semiclassical integral over initial position x_0 and momentum p_0,

$$\Psi_t^{\mathrm{SC}}(x') = \frac{1}{2\pi\hbar}\int dp_0 \int dx_0 C_{xqt} e^{iS_{xqt}/\hbar}\langle x'|p_t x_t \alpha\rangle \times \langle p_0 x_0 \alpha|\Psi_0\rangle. \tag{26}$$

The initial wave function used throughout the study for this potential was $\Psi_0(x) = (2/\pi)^{1/4}\exp[-(x-7.3)^2]$. The Filinov filter was found not to improve the convergence rate in this system. For large values of C, the Filinov filter was too weak to accelerate the convergence rate. For values of C sufficiently small to accelerate the convergence rate, the Filinov filtering effect was found to be too strong and the calculations converged to incorrect results (see Fig. 5).

The second system considers the photodissociation of a generic triatomic molecule and has been previously used as a test case in the calculation of cumulative transition matrix elements.[24] The calculations were performed on a purely dissociative surface for a pseudotriatomic model of CH_2IBr. All relevant parameters, including the form of the potential, can be found in Ref. 24. The initial triatomic wave function used was $\Psi_0(R_s, R_a) \propto \exp[-74.7R_s^2 - 49.4R_a^2]$, with R_s and R_a (the symmetric and asymmetric modes) in atomic units. It was reported in Ref. 24 that the semiclassical calculations of the transition matrix elements converged with 5×10^5 trajectories without the inclusion of the Filinov filter. Similar convergence rates were seen when this calculation was repeated in the present study. As in the case of the 1D anharmonic oscillator, overdamping of the results was seen if any acceleration of the convergence rate was to be achieved using the Filinov filter (not shown).

The third nonchaotic system considered is the nonadiabatic dissociation of ICN.[17,25] The ICN results presented in Refs. 17 and 25 required 2×10^7 trajectories for convergence when making use of the Filinov filter. The initial nuclear wave function used for this system was $\Psi_0(R,\theta) \propto \times\exp[-54.0(R-5.1873)^2 - 29.3\theta^2]$, with R and θ (the I–CN bond length and angle) in atomic units, and the potential energy surfaces are those of Goldfield, Houston, and Ezra.[26] This system is interesting because, even with the inclusion of the Filinov filter, a relatively large number of trajectories were needed to converge the calculation. Since the previous studies on ICN reported positive results when using the Filinov filter, it is important to understand exactly why the Filinov filter, at first glance, seems to be effective in this system. Such an understanding will start with an analysis of possible chaotic regions of the ICN system. By examining exponential divergence of initially neighboring trajectories originating from various points in phase space, we found a small number of chaotic trajectories in ICN. However, all of the chaotic trajectories corresponded to a class of nonphysical solutions that are expected to give no contribution to the semiclassical wave function. Such nonphysical results arise because the Hamiltonian is fictitious, with the nonadiabatic dynamics modeled via a coupling to fake oscillators. Specifically, the ICN Hamiltonian used in the semiclassical simulations is

$$H(R,K,\theta,l,\tilde{\mathbf{p}},\mathbf{x}) = \frac{K^2}{2M} + \frac{l^2}{2MR^2} + \frac{l^2}{2mr^2} + \frac{1}{2}H_{1,1}[\tilde{p}_1\tilde{p}_1 + x_1x_1 - 1] + \frac{1}{2}H_{2,2}[\tilde{p}_2\tilde{p}_2 + x_2x_2 - 1] + H_{1,2}[\tilde{p}_1\tilde{p}_2 + x_1x_2], \tag{27}$$

where $(\tilde{\mathbf{p}},\mathbf{x})$ are oscillators introduced to model the electronic degrees of freedom, (R,θ) and (K,l) are the nuclear coordinates and momenta. The quantities M and m are the I–CN and C–N reduced masses, r is the C–N equilibrium bond length and $H_{k,k'}$ are the diabatic electronic Hamiltonian matrix elements. In the semiclassical methodology used, the initial $(\tilde{\mathbf{p}},\mathbf{x})$ are sampled from harmonic oscillator wave functions. When a particular initial condition satisfies $\tilde{p}_1\tilde{p}_1 + x_1x_1 < 1$, $\tilde{p}_2\tilde{p}_2 + x_2x_2 < 1$, or $\tilde{p}_1\tilde{p}_2 + x_1x_2 < 0$, the nuclear coordinates see negative $H_{1,1}$, $H_{2,2}$, or $H_{1,2}$ energy surfaces, respectively. These trajectories lead to nonphysical behavior since, for example, if $H_{1,1}$ is effectively negative, the nuclear coordinates propagating on this surface will see a large well as $R\to0$ and the I–CN bond length will shrink to zero. All chaotic trajectories observed were found to originate from these nonphysical regions of phase space and should therefore be rejected from the initial sampling distribution.

Once these chaotic trajectories were manually excluded from the initial sampling distribution, the Filinov was found to be no longer effective at accelerating the convergence of the calculation. Thus, the Filinov filter, in the ICN case, does little more than damp out the contribution of the nonphysical chaotic trajectories.

To understand why the Filinov filter is ineffective in these three cases (once the chaotic trajectories are removed from the ICN calculations), consider the behavior of the semiclassical integrand. The calculation of the semiclassical wave function $\Psi^{\mathrm{SC}}(\mathbf{x}',t)$ at a particular point $\mathbf{x}'$ and some time t is considered for each system. The phase and amplitude of the integrand are then plotted as a function of a single integration coordinate while all other coordinates are held constant. Care is taken to ensure that the path taken through the initial phase space by varying only one initial coordinate in this way does in fact pass through a region with high integrand amplitude for the particular final point $\mathbf{x}'$ chosen.

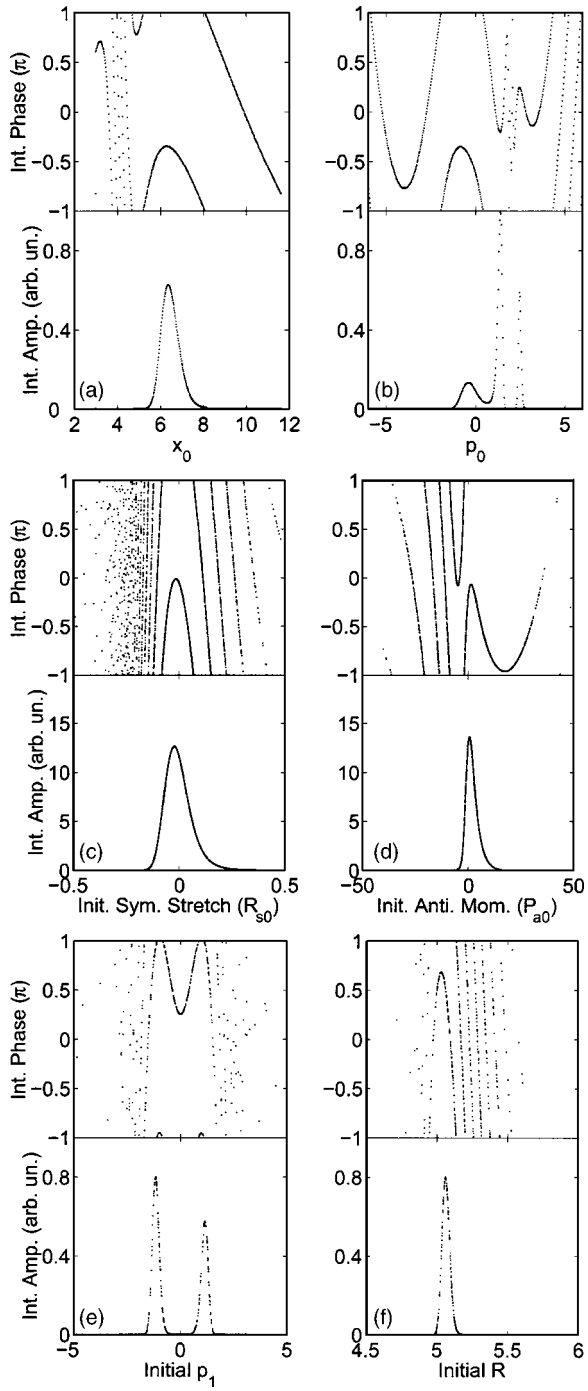

FIG. 1. Integrand phase and amplitude for select paths through phase space. Panels (a) and (b) are for the anharmonic oscillator case shown as a function of x_0 and p_0, respectively. Panels (c) and (d) are for the triatomic case as a function of the initial symmetric stretch R_{s0} and the initial asymmetric momentum P_{a0}. Panels (e) and (f) are for the ICN case as a function of initial p_1 and initial R.

(Otherwise the plot will only reveal the behavior of some irrelevant and negligible low amplitude region of the integrand.)

Figure 1 shows typical results of these calculations for all three systems. Figures 1(a) and 1(b) are for the anharmonic oscillator case propagated to time of $t=2.0$, with the final coordinate being $x'=5$. The integrand is shown [Fig. 1(a)] as a function of x_0 with $p_0=0$ held constant, and Fig. 1(b) as a function of p_0 with x_0 held constant at $x_0=7.3$.

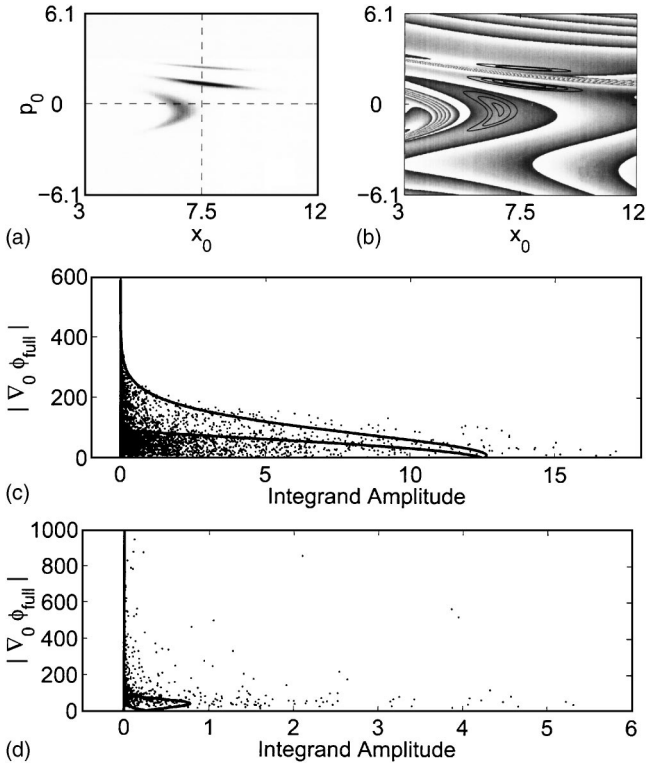

FIG. 2. Relation of the integrand amplitude to the integrand phase. Panel (a) shows the integrand amplitude as a function of both integration coordinates for the anharmonic case. Panel (b) shows the corresponding phase of the integrand (0= white to 2π= black) with a contour plot of the integrand amplitude superimposed for comparison. Next are shown scatter plots of integrand amplitude vs. the full phase gradient for 10^4 trajectories selected from the Monte Carlo sampling distribution for (c) the triatomic case and (b) the ICN case. The line in panel (c) corresponds to the phase gradients of Fig. 1(c) and the line in panel (d) corresponds to the phase gradients of Fig. 1(f). Note that values of $|\nabla_0 \phi_{full}|$ near the zero of the integrand amplitude exceed 40 000 and 80 000 in panels (c) and (d), respectively

Figures 1(c) and 1(d) are for the triatomic system propagated to a time of 20 fs with the final (R_s, R_a) chosen as (0.632, 0.008). Panel (c) in Fig. 1 shows the integrand phase and amplitude first as a function of the initial symmetric stretch coordinate R_{s0}. (Here the other initial coordinates were held fixed at $R_{a0}=-0.010\,222\,6$, $P_{s0}=-9.216\,95$, $P_{a0}=1.5545$.) Panel (d) in Fig. 1 shows the integrand as a function of the initial asymmetric momentum P_{a0} with R_{s0} fixed at 0.033 047 7. Figures 1(e) and 1(f) show results for the ICN system propagated to $t=20$ fs. The integrand behavior is shown in Fig. 1(e) as a function of the electronic momentum p_1 with the remaining coordinates fixed at $R=5.073\,39$, $\theta=-0.000\,294\,587$, $x_1=1.78215$, $x_2=0.477\,678$, $K=27.9355$, $l=-2.328\,62$, and $p_2=-0.682\,554$ and panel 1(f) in Fig. 1 shows the integrand as a function of R where p_1 was now fixed at $p_1=-1.113\,54$. All of these plots show that the regions of high integrand amplitude are accompanied by regions of low phase gradient. The Filinov filter then does not help the convergence of these systems because the regions of high phase gradient, which are down-weighted by the filter, *already contribute negligibly to the integral*.

Motivated by figures of this type, we undertook a general survey of the relation between the phase gradients and the integrand amplitude. Figures 2(a) and 2(b) show the in-

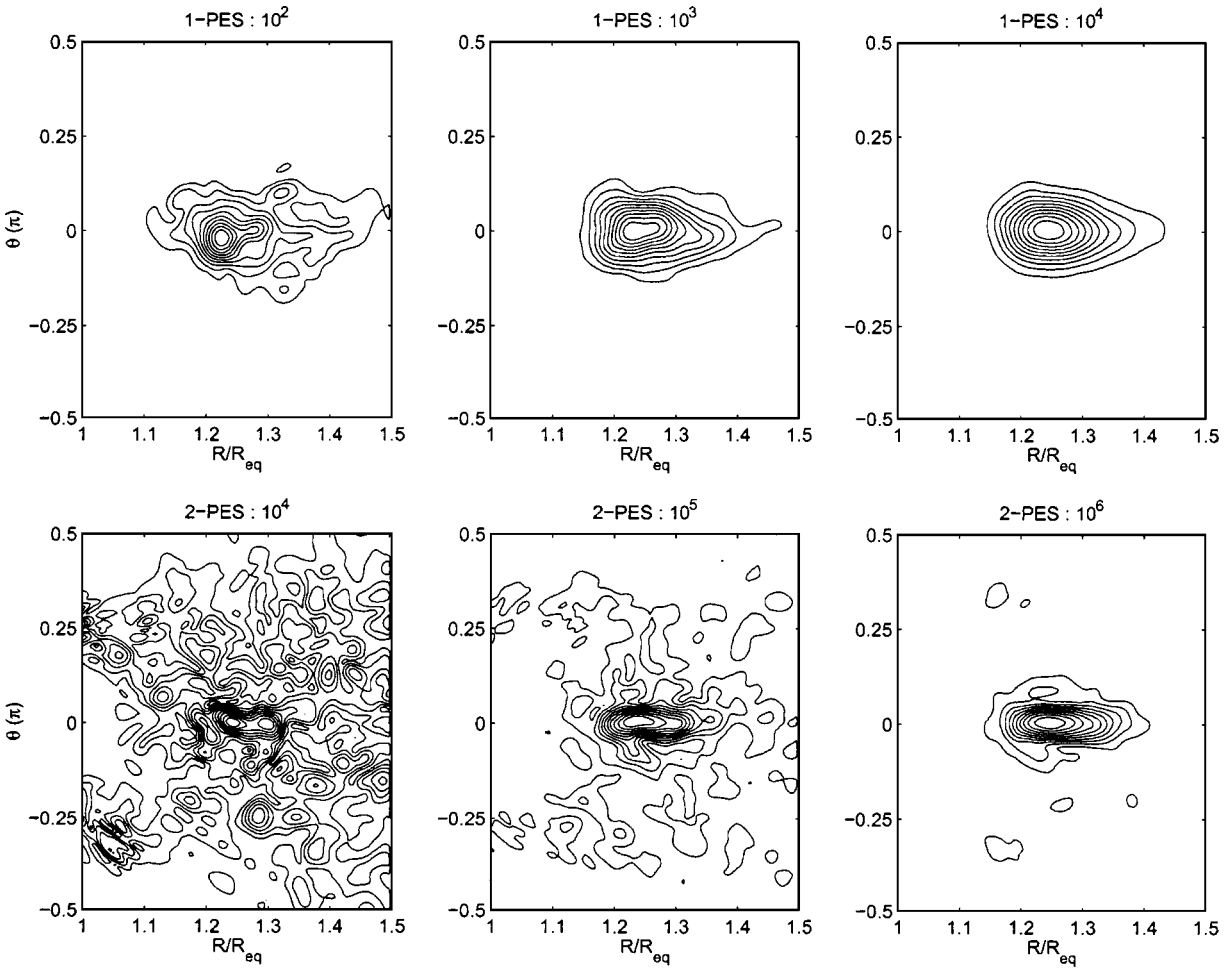

FIG. 3. Contours of the calculated ICN wave function after ionization. Top row: single potential energy surface calculation for 10^2, 10^3, and 10^4 trajectories. Lower row: multiple potential energy surface calculation using nonadiabatic SC-IVR for 10^4, 10^5, and 10^6 trajectories.

tegrand amplitude and phase for the complete integration space of the 1D anharmonic oscillator case. The dashed lines in Fig. 2(a) corresponds to the phase-space paths taken by Fig. 1(a) and 1(b). Notice in Fig. 2(b) that the regions of high integrand amplitude overlap only with regions of low phase gradients.

Unfortunately, visualizing the full phase space for the triatomic and ICN cases is not possible due to the higher dimensionality of these systems. Here we must resort to a statistical sampling of the integration space. Figures 2(b) and 2(c) show scatter plots of integrand amplitude vs the numerically calculated gradient of the full integrand phase $|\nabla_0 \phi_{\text{full}}|$ for 10^4 trajectories randomly selected from the Monte Carlo sampling distribution for the triatomic and ICN systems, respectively. "Full integrand phase" means the integrand phase including the contribution from the prefactor C_{pqt}. No initial coordinates were held fixed. The curve in Fig. 2(c) corresponds to the phase gradients of Fig. 1(c) and is shown for comparison against the scatter plot. Similarly, the line in Fig. 2(d) corresponds to the phase gradients of Fig. 1(f). Note that the *y* axes were truncated for clarity; the phase gradients near the zero integrand amplitude region go up as high as 40 000 for the triatomic case and 80 000 for ICN. This shows that the behavior seen in Fig. 1 is indeed representative of the behavior of the full integrands, with no relation between large integrand amplitude and large phase gradients.

There remains the question as to why the ICN calculation takes two orders of magnitude more trajectories than does the model one-surface triatomic. When we carried out single surface simulations of ICN using either of the two electronic surfaces i.e., without the nonadiabatic SC-IVR formalism), they were found to require the same number of trajectories for convergence as did the model triatomic. Thus, the convergence difficulties are not intrinsic to the ICN potential energy surfaces, but instead originate from the nonadiabatic SC-IVR procedure. It seems plausible to assume that the coupled electronic degrees of freedom are perhaps introducing difficulties. However, this is incorrect. Simulations of the ICN dissociation using the nonadiabatic formalism, but with the coupling turned off ($H_{1,2}=0$) still took $\sim 10^7$ trajectories for convergence. This is clearly strange, since without the coupling terms the electronic degrees of freedom reduce to two extra simple harmonic oscillators for which the SC-IVR evaluation should require a minimal amount of trajectories. So from where do the convergence difficulties arise upon inclusion of the electronic degrees of freedom?

Figure 3 shows contours of the wave function calculated for a single-surface ICN dissociation (top row) and the two-

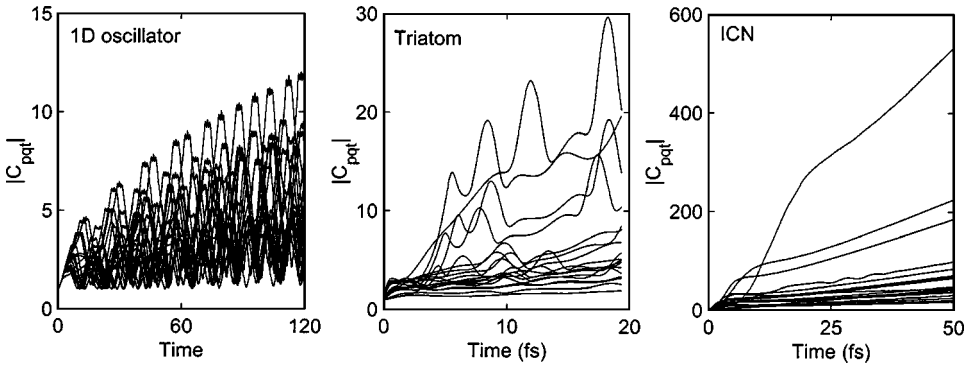

FIG. 4. Time evolution of C_{pqt} for a few sample trajectories showing the characteristic behavior for each system.

surface ICN with coupling (bottom row). All the classical trajectories for the one-surface system end up near the final position of the wave function and hence all can contribute in a useful way to the integral. Both the converged wave function, and the wave function computed with a small number of trajectories occupy similar spatial regions. For the two-surface simulations, however, the spread in the final position of the classical trajectories is much larger than the spread of the final converged wave function. Indeed, the ratio of the spread in the trajectories to the spread in the final wave function is estimated to be roughly 10:1. This large spread of the classical trajectories arises from the fact that the Hamiltonian for the nonadiabatic SC-IVR method introduces an average over many different weights of the nuclear potentials so that trajectories propagate on a distribution of effective potential energy surfaces. Furthermore, all the classical trajectories for the two-surface system contribute to the large spread with about equal order of magnitude amplitude. This additional spread of the trajectories, compared to the converged wave function, can be clearly seen in the plots of the wave function for low numbers of trajectories where there are contributions that fill the entire spatial map. Hence, the convergence difficulty for two-surface ICN is caused by the need to average out most of the large spread in position (and hence most of the trajectories) to zero. The same interpretation holds in the momentum spread of the nuclear coordinates as well, where the classical trajectories span a region that is again much larger than the final converged. A "wasted volume" of trajectories in both position and momentum space of about 10:1 in each gives a wasted volume in the full integration phase space of about 100:1, which agrees well with the extra computation effort needed to converge the two-surface ICN as compared to the one-surface ICN.

This section concludes with a brief consideration of the time evolution of the semiclassical prefactor for these systems as well as an explicit demonstration of the overdamping caused by the Filinov filter for the calculation of the autocorrelation function of the 1D anharmonic oscillator. This will be of use for comparison with the chaotic systems considered in the following section. Figure 4 shows the prefactor C_{pqt} for a representative set of 20 trajectories for each of the three systems considered in this section. All three systems show at most a polynomial increase in the magnitude of the prefactor with time. This polynomial increase arises from the fact that the prefactor is a polynomial function of the stability matrix elements which, for regular dynamics, scale as a polynomial in time. This polynomial scaling of the prefactor is a key requirement for the convergence of the semiclassical integrals without any filtering of the integrand and, as will be seen in the following section, is in stark contrast with the behavior of the prefactor for chaotic systems.

Figure 5(a) shows the calculated autocorrelation function for the 1D anharmonic oscillator system obtained using the Filinov filter with a variety of filter settings. Figure 5(b) plots the quantum result for comparison. When using a mild filter parameter (i.e., large values of C) or no filter at all, the semiclassical autocorrelation function quite closely resembles the quantum result for the full time range, but no acceleration of the convergence rate is obtained. However, as the filter parameter becomes more aggressive (i.e., smaller C values), the accelerated convergence rate is accompanied by a semiclassical autocorrelation function that becomes artificially damped out for large times.

The long-time structure of the autocorrelation is indicative of resonances in the system and is responsible for sharp features in the corresponding energy spectrum $I(E)$. The overdamping seen in the semiclassical autocorrelation function will then manifest itself in a broadening of the resonance peaks in the corresponding spectrum $I(E)$, significantly reducing the spectral quality. Hence, there is a *disadvantage* to using the Filinov filter in this case.

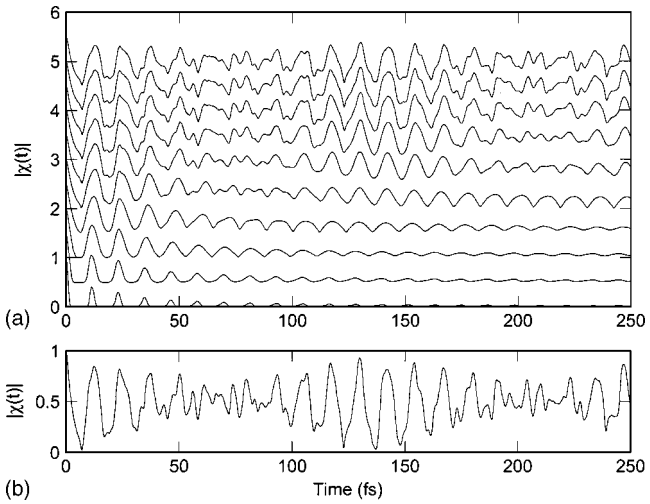

FIG. 5. The calculated autocorrelation function $\chi(t)$ for the 1D anharmonic oscillator system. (a) Semiclassical results for $C=5^{-2},5^{-1},5^{0},5^{1},\ldots,5^{6}$ and for no Filinov filter, from bottom to top. (b) Quantum result.

IV. CHAOTIC SYSTEMS

Consider now the more interesting case of chaotic systems. Here both advantages and drawbacks of using the Filinov filter to accelerate the convergence of the semiclassical calculations will become increasingly evident.

Four model systems will be considered. The first is a two surface nonadiabatically coupled system used by Stock and Thoss.[20] This model exhibits regular quantum dynamics (with respect to such measures as the energy level spacings) but shows chaotic classical dynamics for large times which, unlike the ICN case of the preceding section, cannot be trivially removed from the computation. The Hamiltonian is given by

$$H = \frac{\omega}{2}(P^2 + X^2)\mathbf{1} + \begin{bmatrix} V_{11} & V_{12} \\ V_{12} & V_{22} \end{bmatrix}, \tag{28}$$

where $V_{11} = -V_{22} = \Delta/2 + \kappa X$ and $V_{12} = g$. In keeping with Ref. 20, we use the parameters $\Delta = 1$, $g = 0.2\Delta$, $\omega = 0.1\Delta$, and $\kappa = 0.05\Delta$. The initial wave packet $\Psi_0(X, l)$ used was the ground state wave function of the single oscillator ($H = \omega/2[P^2 + X^2]$) placed on the ground electronic surface, $l = 1$.

The next two systems are classic models of both quantum and classical chaos, namely, the quartic oscillator and the Henon–Heiles system. Both of these systems have been studied using SC-IVR, with some form of integral filter techniques used to converge the results.[15,16,18,19,27] All of the studies reported beneficial attributes of the Filinov filter. We repeat these calculations here and identify both advantages and limitations of such filtering techniques.

The quartic oscillator is defined by the Hamiltonian

$$H = \frac{1}{2}P_x^2 + \frac{1}{2}P_y^2 + \frac{1}{2}x^2y^2 + \frac{1}{4}\beta(x^4 + y^4) \tag{29}$$

with $\beta = 0.01$. The initial wave packet used was $\Psi_0(x, y) \propto \exp[-0.5x^2 - 0.5(y - 8.32)^2]$. The Henon–Heiles system has the Hamiltonian

$$H = \frac{1}{2}P_x^2 + \frac{1}{2}P_y^2 + \frac{1}{2}(x^2 + y^2) + \lambda(x^2y - y^3/3) \tag{30}$$

with $\lambda = 0.1118$. The initial wave packet used for this system was $\Psi_0(x, y) \propto \exp[-0.5(x - x_0)^2 - 0.5(y - y_0)^2 + ixP_{x0} + iyP_{y0}]$ with $x_0 = 0$, $y_0 = -1.914$, $P_{x0} = 3.976$, and $P_{y0} = 0.961$.

The fourth chaotic example involves the calculation of the absorption cross section of 2D planar H_2O in the second absorption band, which occurs via a transition from the $(X\,^1A')$ ground electronic surface to the $(\tilde{B}\,^1A')$ excited electronic surface. This model is similar to the dissociative systems considered in the preceding section except that the excited state potential energy surface contains a well in which the classical trajectories can oscillate and undergo chaotic dynamics prior to dissociation. The two coordinates considered are one HO–H bond length R and the HO–H bend γ. The HO fragment was assumed to be a rigid diatom with bond length of $r_{eq} = 1.835a_0$. The excited surface $V(R, \gamma)$ used is that of Segev and Shapiro.[28] The Hamiltonian of the system on the excited surface for total angular momentum $J = 0$ is

$$H = \frac{P_R^2}{2\mu_R} + \frac{j^2}{2\mu_R R^2} + \frac{j^2}{2I_{\mathrm{OH}}} + V(R, \gamma), \tag{31}$$

where j is the angular momentum associated with the bend mode γ, $\mu_R = m_{\mathrm{H}}(m_{\mathrm{H}} + m_{\mathrm{O}})/(2m_{\mathrm{H}} + m_{\mathrm{O}})$ and $I_{\mathrm{HO}} = r_{eq}^2 m_{\mathrm{H}} m_{\mathrm{O}}/(m_{\mathrm{H}} + m_{\mathrm{O}})$. The initial state used was $\Psi_0(R, \gamma) \propto \exp[-11.73(R - r_{eq})^2 - 5.98(\gamma - \gamma_0)^2]$, with γ measured in radians and $\gamma_0 = 104°$. The majority of the trajectories for this initial state dissociate after one or two oscillations but the remaining trajectories undergo complicated chaotic motion in the potential well for many oscillations before dissociation. A small number of trajectories remain trapped in the well, exhibiting pseudobound chaotic dynamics.

The first point of interest with these systems relates to the behavior of the prefactor C_{pqt}. A set of 20 representative trajectories are plotted in Fig. 6 for each of the four chaotic systems using, unlike Fig. 4, a logarithmic vertical scale. All four systems exhibit some trajectories with exponentially increasing prefactors. These appear as more or less linearly increasing functions on the logarithmic plots and are the chaotic contributions. This is the root of the convergence difficulties in chaotic systems using Monte Carlo sampling. Converging the integral for $\chi(t)$, with exponential growth of the integrand as a function of time, requires an exponentially increasing number of trajectories with increasing time.

To clearly see the advantages of using the Filinov filter for chaotic systems we first calculate $\chi(t)$. Figures 7 and 8 plot the autocorrelation functions $\chi(t)$ for the quartic oscillator and the H_2O systems, respectively. Panels (a) in both Figs. 7 and 8 plot the SC-IVR $\chi(t)$ for various values of the Filinov strength parameter C (see captions) while panels (b) plot the fully quantum $\chi(t)$ calculated using FFT grid-based methods. The quartic oscillator simulations used 10^7 trajectories while the H_2O simulations used 2×10^6 trajectories. In the absence of any filtering as well as for weak filter strength (i.e., large C), the semiclassical $\chi(t)$ grows exponentially for large times due to the exponentially increasing C_{pqt}. The semiclassical calculation of these autocorrelation functions then has no chance of converging over an arbitrarily large time range without some form of integral conditioning due to the exponential growth of the semiclassical prefactor. For more aggressive filter settings (i.e., smaller values of C), the autocorrelation functions are seen to have converged but now there is clear overdamping at large times when compared to the quantum result, as was seen in the 1D anharmonic oscillator case (Fig. 5). In practice, then, the Filinov filter should be tuned to damp out the exponentially increasing contributions while overdamping as little as possible, with the optimum choice of C being as large as possible while still permitting numerical convergence of the calculation. Autocorrelation functions for the Stock and Thoss systems as well as the Henon-Heiles system are shown in the following discussion.

It is important to stress here that, however, accurate (or inaccurate) the result of the calculation using the Filinov filter happens to be, its inclusion makes the convergence possible despite the underlying exponential growth of the semiclassical prefactor and represents an exponential acceleration of the convergence rate. This is the main benefit of the Fili-

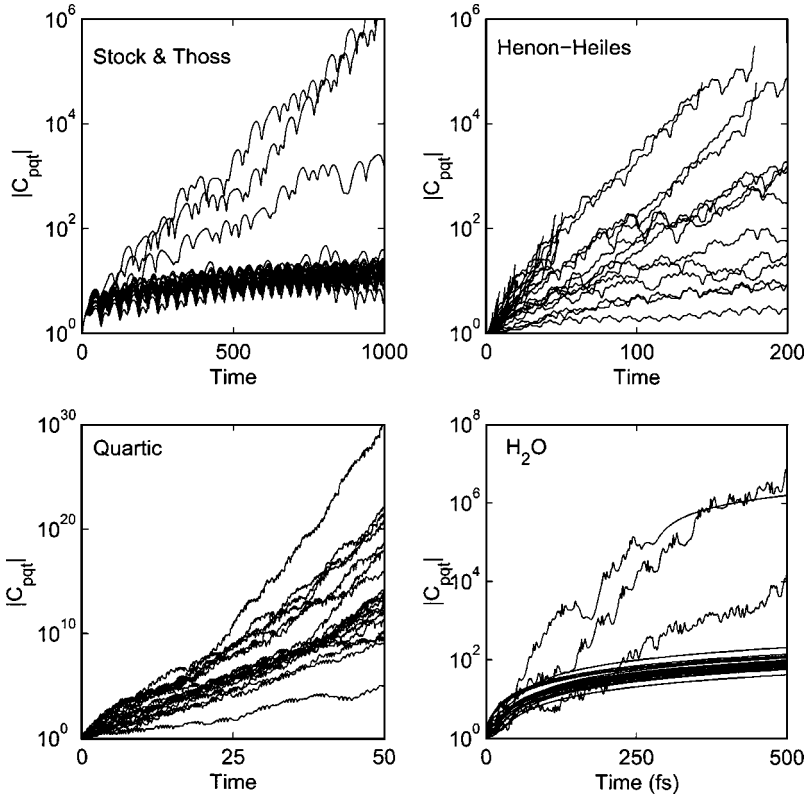

FIG. 6. Time evolution of C_{pqt} for a few sample trajectories showing the characteristic behavior for each system.

nov filter in the case of chaotic dynamics. The remaining question, then, is exactly how accurate are the results when the Filinov filter is used to converge the calculations?

To address this question we consider the energy spectrum of these systems, as calculated from the Fourier transform of $\chi(t)$ for the optimal value of C chosen as just outlined. We consider the four chaotic cases in order of increasing difficulties with the Filinov filter. The spectrum of the Stock and Thoss model is shown in Fig. 9 for both the full quantum and the semiclassical calculations (shown inverted). The semiclassical results used a Filinov setting $C=10^6$ and 10^5 trajectories. The inset shows, from top to bottom, the autocorrelation function calculated with no filter, with $C=10^6$ (the optimal value for the number of trajectories used) and with $C=10^2$ which leads to overdamping, and finally the full quantum autocorrelation function. Here the autocorrelation function calculated with the optimal Filinov parameter matches well the quantum result. Returning to the calculated spectra, we see that the semiclassical spectrum with the optimal Filinov parameter agrees quite well with quantum spectrum for this system. Thus, the Filinov filter is having a positive effect in this case, filtering out the unwanted exponential growth of the integrand. It should be noted here that the energy spacings for this model (nearly harmonic) suggest that the system is dominated by regular quantum dynamics. Furthermore, when looking at the repre-

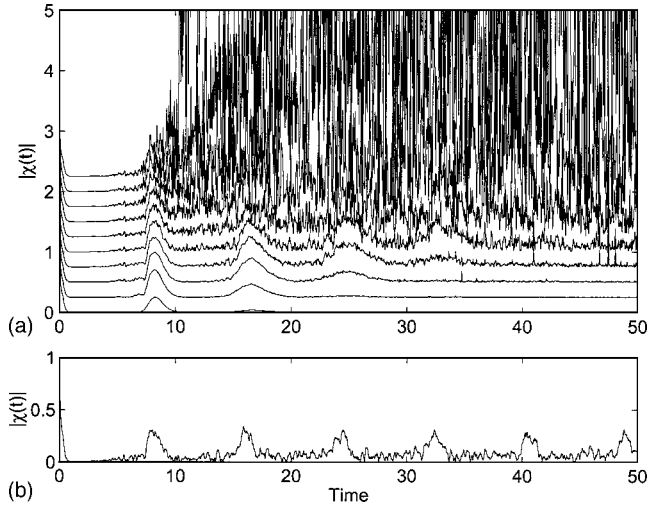

FIG. 7. The autocorrelation function $\chi(t)$ for the quartic oscillator. (a) Semiclassical results for $C=10^2, 10^4, 10^6, \ldots, 10^{18}$ and for no Filinov filter, from bottom to top. (b) Quantum result.

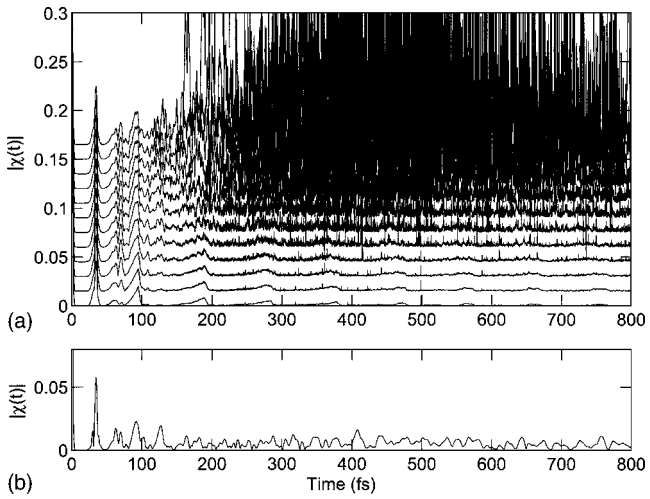

FIG. 8. The calculated autocorrelation function $\chi(t)$ for the H_2O system. (a) Semiclassical results for $C=10^3, 10^4, 10^5, \ldots, 10^{13}$ and no Filinov filter, from bottom to top. (b) Quantum result.

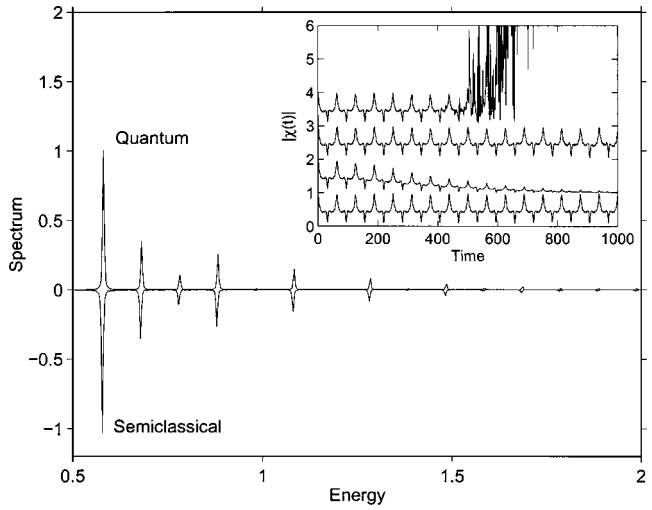

FIG. 9. Quantum (top) and semiclassical (inverted) spectrum $I(E)$ for the Stock and Thoss system. Inset: semiclassical and quantum autocorrelation functions (see text.)

sentative sample of trajectories shown in Fig. 6 there are clearly two classes of behavior, one exhibiting exponential growth of C_{pqt} and the other exhibiting polynomial growth. It appears then that the Filinov is correctly filtering out the chaotic contributions of the underlying classical dynamics which, judging by the regular energy spacings of the quantum spectrum, should not have a significant effect on the quantum dynamics anyway.

Next consider the calculated spectra of the Henon–Heiles system. This is an interesting case because the initial wave packet used overlaps with both regular and chaotic regions of the classical phase space so that the quantum dynamics involves both regular and irregular eigenstates. (The classical dynamics, however, is only mildly chaotic in comparison with the two examples to follow, the quartic oscillator and the H_2O system.) The quantum and semiclassical (10^6 trajectories) spectra are shown in Fig. 10 for two values of the Filinov parameter: panel (a) uses $C=10^6$ while panel (b) uses $C=10^2$. At energies below $E_c \sim 9.1$, the threshold for chaotic classical dynamics, both spectra agree very well. For these energies, the classical dynamics is nonchaotic and the

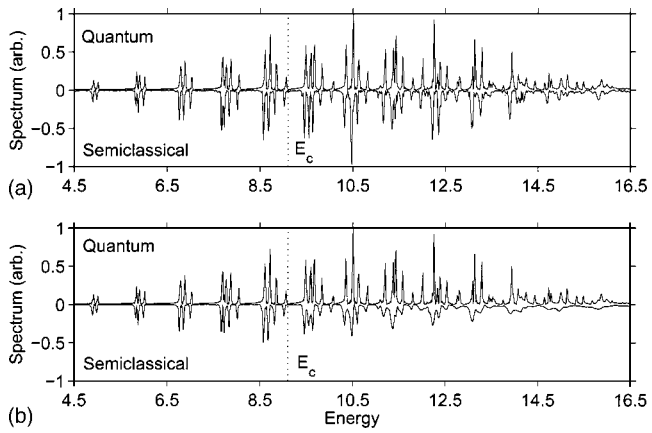

FIG. 10. Quantum (top) and semiclassical (inverted) spectrum $I(E)$ from the Henon–Heiles system. The semiclassical calculations used the Filinov setting of $C=10^6$ [panel (a)] and $C=10^2$ [panel (b)].

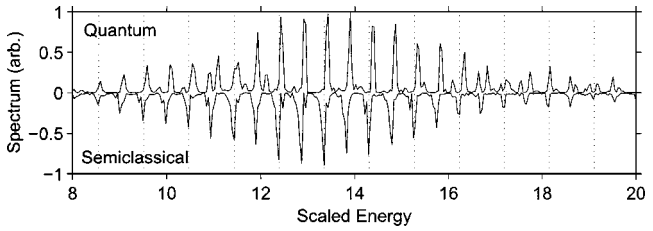

FIG. 11. Quantum (top) and semiclassical (inverted) spectrum $I(E)$ of the quartic oscillator.

quantum eigenstates are regular. Above E_c, the dynamics is increasingly chaotic with energy and the majority of the quantum eigenstates quickly take on an irregular or chaotic character.[29,30] The $C=10^6$ semiclassical results still agree quite well with the quantum results in this region and only start to diverge noticeably for the highest energies plotted ($E>14.5$–16.5). The case is, however, not the same when the stronger filtering $C=10^2$ is used, as would be necessary to converge a calculation when, for example, only a smaller number of trajectories is available. For this case, the quantum and semiclassical spectra are seen to correspond less and less above E_c with the semiclassical spectrum missing much of the fine structure and sharpness of the peaks seen in the high-energy quantum spectrum. As mentioned in the preceding section, the broadening of the energy peaks has its origin in the overdamping of the long-time autocorrelation function. The semiclassical spectrum then shows that the high energy chaotic dynamics is strongly affected by overdamping while the low-energy nonchaotic dynamics remains relatively untouched. These two cases then give a clear picture of the overdamping that results when strong filtering is required to force early convergence of a semiclassical calculation.

The quantum and semiclassical ($C=10^8$) spectra for the quartic oscillator are shown in Fig. 11. As is the convention in the literature for this system, we plot the spectra vs the scaled energy $(2E)^{3/4}$. Here the large scale features (general width of the spectra, average peak spacing) of the two spectra agree quite well. However, many of the small scale features seen in the quantum spectrum are lost in the semiclassical result; e.g., a number of the quantum peaks are doublets, but show up as single peaks in the SC-IVR spectrum. The vertical dotted lines denote eigenergies calculated in Ref. 31 which follow from an adiabatic separation of the two degrees of motion of the system. These results represent essentially uncoupled eigenstates of the oscillator. Although these eigenenergies are only approximate, as can be seen from the quantum spectrum, they all match the semiclassical peaks quite well. Furthermore, the remaining peaks of the semiclassical spectrum, which fail to exhibit the doublet structure of the quantum spectrum, appear to be spaced by the near-harmonic spacing suggested by the uncoupled eigenenergies. These findings suggest that the semiclassical spectrum converged using the Filinov filter is missing the coupled character of the correct eigenstates and may be forcing artificially regular spacing statistics on the energy spectrum.

Figure 12 shows the calculated low-energy H_2O spec-

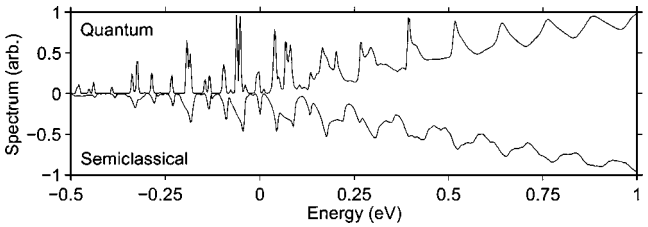

FIG. 12. Near-barrier bound states and low-energy continuum spectrum $I(E)$ of the H_2O system for the quantum and semiclassical cases with $C=10^6$.

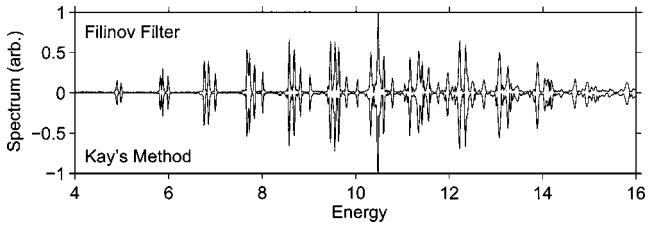

FIG. 14. Spectra of the Henon–Heiles systems calculated using the Filinov filter and Kay's method.

trum for the quantum case and the semiclassical case with $C=10^6$. The sharpness of the continuum resonances seen in the quantum case is lost in the semiclassical spectrum. Furthermore, the energy peak resolvability is much worse in the bound state spectrum of the semiclassical results as compared to that of the quantum results. Again, this is because the semiclassical autocorrelation function is overdamped in using the Filinov filter and the long-time behavior is suppressed, causing a broadening of the peaks.

V. ALTERNATE FILTERING METHODS

The large majority of the SC-IVR literature dealing with chaotic dynamics and integral conditioning techniques has centered around some version of the Filinov filter.[1,10,15,18,23] However, Kay[19] has introduced a much more *ad hoc*, yet nonetheless successful, method of dealing with contributions arising from chaotic trajectories. For a recent application of Kay's method see Ref. 32. We now compare these two methods and argue that they operate on an essentially equivalent level of approximation.

In Kay's method,[19] a given trajectory is included in the semiclassical integral up until the magnitude of the prefactor $|C_{pqt}|$ grows larger than some preset function of time. Here we use the criterion to keep a trajectory until $|C_{pqt}|>C_{\mathrm{cut}}$ where C_{cut} is a constant controlling the strength of the filtering using this method.

Figure 13 plots the autocorrelation function for the Henon–Heiles system calculated using the Filinov filter and Kay's method for a variety of filter strengths. From these plots we see very similar behavior in the two methods as the filter parameters are varied: for weak filtering, the autocorrelation function grows exponentially for large times and for stronger filtering, the autocorrelation is prematurely damped out. Figure 14 shows the corresponding spectrum for optimal filter parameters using the Filinov ($C=10^6$) and Kay's method ($C_{\mathrm{cut}}=10^{2.5}$). Both methods are seen to give essentially equivalent approximations to the full quantum spectrum (see Fig. 10).

Some understanding of the connection between these two methods can be obtained by considering the relation between the phase gradient and the prefactor. Figure 15 plots $|\nabla\phi|^2$ vs $|C_{pqt}|$ for a random sample of 100 trajectories used to calculate the autocorrelation function. These two parameters are seen to be strongly correlated and almost fall on a straight line in the log-log plot. This linear relationship on the log scale follows from the fact that both the phase gradient and the prefactor are polynomial functions of the stability matrix elements. The slope of the line gives the polynomial relation between these two values.

Figure 16 plots the filter functions for both methods on a

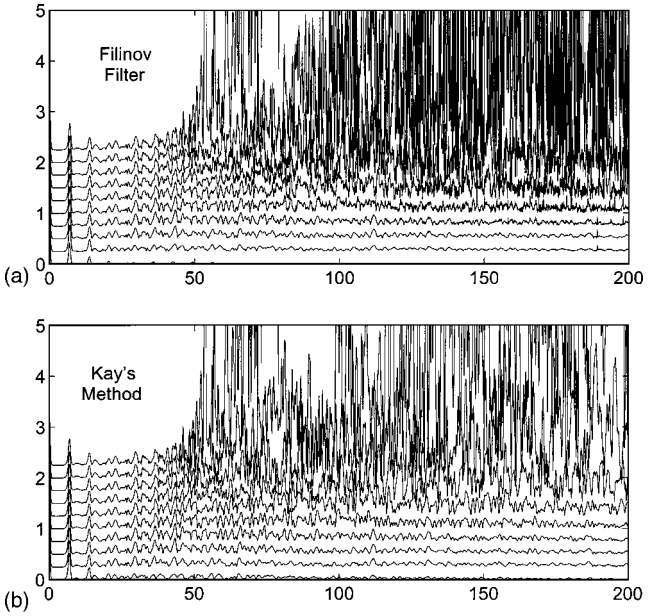

FIG. 13. Autocorrelation functions calculated using (a) the Filinov filter for $C=10^0,10^2,10^4,\ldots,10^{16}$ and for no filter, and (b) Kay's truncation method using $C_{\mathrm{cut}}=10^1,10^{1.5},10^2,\ldots,10^5$ and for no filter.

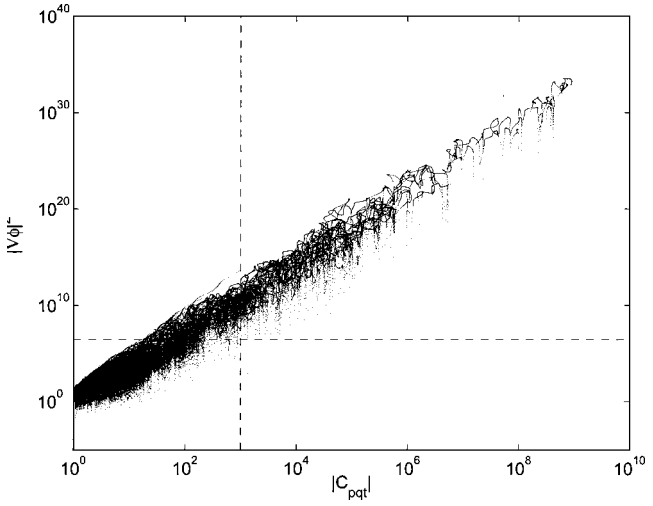

FIG. 15. Scatter plot of the phase gradient $|\nabla\phi|^2$ used in the Filinov filter vs the magnitude of the prefactor $|C_{pqt}|$ used in Kay's method, showing the polynomial relationship between the two parameters. Dashed lines show the effective cutoff values for the two filters as used in Fig. 14.

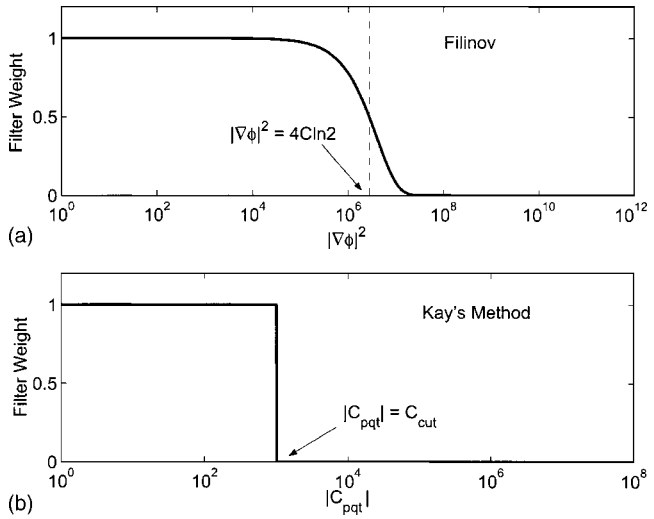

FIG. 16. Weighting functions used for (a) the Filinov filter and for (b) Kay's method.

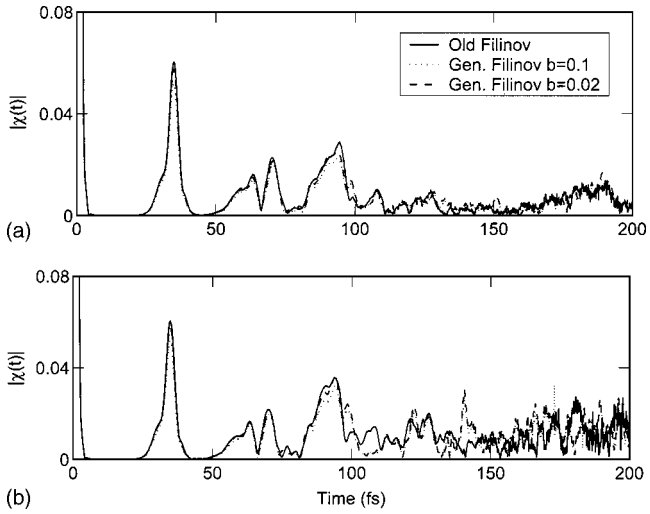

FIG. 17. Semiclassical calculations of the autocorrelation function up to times of 200 fs for both the simple (old) and generalized Filinov filters (see text for details.)

log scale to match Fig. 15. The filter for Kay's method is simply a step function in the prefactor with cutoff $|C_{pqt}| = C_{\mathrm{cut}}$ while the filter function for the Filinov method is a smoothed step function with effective cutoff at $|\nabla\phi|^2 = 4C\ln 2$ (point where filter weight is 0.5). These two cutoff values are plotted as vertical and horizontal dashed lines in Fig. 15. From this plot it can be seen that the two filter methods are both simply rejecting trajectories with integrand amplitude greater than C_{cut}: Kay's method does this directly while the Filinov method does so indirectly through the polynomial relationship between $|\nabla\phi|^2$ and $|C_{pqt}|$. They are therefore both filtering out essentially the same set of trajectories, and hence give similar approximations to the dynamics.

Further to the equivalence of the Filinov and Kay's method, it should be noted that many of the conclusions reached in the preceding section regarding the overdamping of strong chaotic dynamics in the semiclassical calculations when using strong Filinov filtering are essentially identical to the conclusions reached by Kay when he initially analyzed his truncation method.[19]

The literature also offers a few more refined versions of the Filinov filter than that presented in Sec. II C. The first version[1,10,18] differs only in that it keeps higher order terms in the Taylor expansion in going from Eq. (17) and (18). These terms, however, only affect the final form of the Filinov filter by the appearance of an additional preexponential term that is polynomial in the stability matrix elements. The filtering power of the Filinov, however, lies in the exponential weighting term $e^{-|\nabla\phi|^2/4C}$ and the additional preexponential term arising in the higher order Filinov methods did not improve the method when tested in the present study. In fact, the results deep into the region of exponential growth differed negligibly when compared with both the simple Filinov of Sec. II C as well as Kay's truncation method, confirming that the preexponential term is of little help to the Filinov in converging the long-time dynamics.

A second alternate Filinov transformation of the semiclassical initial value representation, called the generalized Filinov transform, has also been proposed.[23] This generalized Filinov filter was shown[23] to accelerate the convergence of a multidimensional (up to $N=10$) Henon–Heiles-type potential as well as a pyroxene model. There the main focus was to converge the short-time autocorrelation function with as few trajectories as possible. A complete description of the method can be found in Wang, Manolopoulos, and Miller[23]. The essential difference between the generalized Filinov technique and that outlined in Sec. II C is that an alternate representation of unity is inserted into the initial integrand [see Eqs. (16) and (17)]. The representation of unity used in the generalized Filinov filter has a linear term in the exponent in addition to the quadratic term. The first parameter, called a, is the analog of the C parameter used in the standard Filinov filter and controls the width of the Gaussians in the expansion of unity. The second parameter, called b, controls the strength of the linear term and can take on values of 0–1, but small values (typically $b<0.2$) were recommended.

We have applied the generalized Filinov filter to the 2D H_2O model to see if it can accelerate the calculation of the long-time dynamics. Figure 17 shows the results of semiclassical calculations of the autocorrelation function up to times of 200 fs for both the standard and generalized Filinov filters. [Figure 17(a) uses $a=C=10^6$ and Fig. 17(b) uses $a=C=10^9$.] Both (a) and (b) show results of the generalized Filinov filter for b values of 0.1 and 0.02. The autocorrelation function at times larger than 100 fs shows noise fluctuations that are on the same order when using the standard Filinov or the generalized Filinov filter. Changing the a and C parameters shows that these fluctuations are damped (or undamped) by roughly the same amount for either the standard or generalized Filinov filters. The only effect of the b parameter for the generalized Filinov is to cause overdamping over the entire time range. This can be most easily seen by looking at the 40 fs peak. The cases for the standard Filinov and the generalized Filinov with $b=0.02$ overlap quite well, but the case with $b=0.1$ for the generalized Filinov is seen to be smaller in amplitude. Indeed, the only difference between the $b=0.1$ and $b=0.02$ cases is that the results for the former are

overdamped. It seems that the generalized Filinov filter is no better than the standard Filinov at accelerating the convergence of the long-time dynamics for H_2O, and furthermore, it introduces new sources of overdamping when b becomes too large. These observations were supported by additional simulations on H_2O that we carried out using a wider variety of a and b parameters.

VI. CONCLUSIONS AND RECOMMENDATIONS

When we began this work, we adopted the accepted view that the Filinov filter serves a positive role in semiclassical initial value representation calculations. This work has shown this to be only partially correct. First, in the case of nonchaotic systems, the inclusion of the Filinov does little more than cause overdamping, if any acceleration of the convergence rate is to be achieved. The reason for this lies in the lack of large phase oscillations in the regions of large integrand amplitude, the numerical difficulty that the Filinov filter is designed to alleviate. Second, in the case of chaotic dynamics, where regions of large phase oscillations concomitant with regions of large integrand amplitude do abound, the inclusion of the Filinov filter does make the convergence of the semiclassical integrals possible. However, while the filtered results do a good job at representing regular quantum dynamics, the quantum chaotic behavior was seen to be easily overdamped if strong filtering is required to converge the calculations.

The demonstrated equivalence between the Filinov filter and Kay's truncation method suggests a possible shift in integral conditioning techniques. The Filinov method, especially the higher order methods discussed in Sec. V, is rather complicated and cumbersome as compared to the simplicity of Kay's truncation method. Furthermore, if one looks closely at the results of the two methods (Fig. 13), Kay's method is seen to give a smoother approximation near the convergence limit. This is due to the fact that Kay's method rejects *all* trajectories larger than C_{cut} while the weighting function of the Filinov method lets a few trajectories through with larger amplitudes, which causes larger residual fluctuations. If the equivalence of the two methods goes unchallenged, these two points seem to suggest Kay's method as the better of the two integral conditioning techniques for semiclassical initial value representation methods.

Based on these observations, we offer the following recommendations: (i) In the case of regular classical dynamics, the use of filtering techniques is not required, and should therefore be avoided at the risk overdamping of the results. (ii) In the case of classically chaotic dynamics, filtering should be used to make possible the convergence of the calculations, but with the understanding that any strongly quantum chaotic character will be misrepresented. (iii) Filinov-based filtering methods can be replaced in all cases by the simpler truncation method of Kay.

The fact that the regions of high phase gradients have been shown to be linked to regions of low integrand amplitude for the non-chaotic systems means that the Filinov weight factor [see Eq. (19)] is indeed well suited to identify the regions of high integrand amplitude. One might then consider returning to the original idea proposed by Makri and Miller[10,11]. Incorporating the Filinov weight factor into some optimized Monte Carlo sampling procedure[33] could prove to be quite useful. Furthermore, the present usage of the Filinov filter for chaotic systems requires one to sample the chaotic regions and essentially set these contributions to zero via the weighting factor which leads to a large amount of 'wasted' Monte Carlo integration points. Using the Filinov in some importance sampling technique could in this case also prevent searching through this wasted integration volume leading to yet more efficient Monte Carlo methods. Such importance sampling techniques, however, would not be expected to correct the problem of misrepresentation of the strong quantum chaotic dynamics demonstrated herein. It remains an open question if the unfiltered SC-IVR method, if allowed to run to convergence on some hypothetical super computer, could recover the correct quantum chaotic dynamics, or if this chaotic behavior is indeed lost in the semiclassical approximation altogether.

ACKNOWLEDGMENT

The authors acknowledge support of this research from the Natural Sciences and Engineering Research Council of Canada.

[1] W. Miller, J. Phys. Chem. A **105**, 2942 (2001).
[2] M. F. Herman and E. Kluk, Chem. Phys. **91**, 27 (1984).
[3] E. Kluk, M. F. Herman, and H. L. Davis, J. Chem. Phys. **84**, 326 (1986).
[4] M. F. Herman, J. Chem. Phys. **85**, 2069 (1986).
[5] G. Campolieti and P. Brumer, Phys. Rev. A **50**, 997 (1994).
[6] K. G. Kay, J. Chem. Phys. **100**, 4377 (1994).
[7] K. G. Kay, J. Chem. Phys. **100**, 4432 (1994).
[8] V. S. Filinov, Nucl. Phys. B **271**, 717 (1986).
[9] R. D. Coalson, D. L. Freeman, and J. D. Doll, J. Chem. Phys. **85**, 4567 (1986).
[10] N. Makri and W. H. Miller, Chem. Phys. Lett. **139**, 10 (1987).
[11] N. Makri and W. H. Miller, J. Chem. Phys. **89**, 2170 (1988).
[12] B. W. Spath and W. H. Miller, J. Chem. Phys. **104**, 95 (1996).
[13] B. W. Spath and W. H. Miller, Chem. Phys. Lett. **262**, 486 (1996).
[14] X. Sun and W. H. Miller, J. Chem. Phys. **108**, 8870 (1998).
[15] M. F. Herman, Chem. Phys. Lett. **275**, 445 (1997).
[16] B. R. McQuarrie and P. Brumer, Chem. Phys. Lett. **319**, 27 (2000).
[17] E. A. Coronado, V. S. Batista, and W. H. Miller, J. Chem. Phys. **112**, 5566 (2000).
[18] A. R. Walton and D. E. Manolopoulos, Mol. Phys. **87**, 961 (1996).
[19] K. G. Kay, J. Chem. Phys. **101**, 2250 (1994).
[20] G. Stock and M. Thoss, Phys. Rev. Lett. **78**, 578 (1997).
[21] X. Sun and W. H. Miller, J. Chem. Phys. **106**, 6346 (1997).
[22] H. D. Meyer and W. H. Miller, J. Chem. Phys. **70**, 3214 (1979).
[23] H. Wang, D. E. Manolopoulos, and W. H. Miller, J. Chem. Phys. **115**, 6317 (2001).
[24] V. S. Batista and P. Brumer, J. Chem. Phys. **114**, 10321 (2001).
[25] V. S. Batista and P. Brumer, J. Phys. Chem. A **105**, 2591 (2001).
[26] E. M. Goldfield, P. L. Houston, and G. S. Ezra, J. Chem. Phys. **84**, 3120 (1986).
[27] G. Campolieti and P. Brumer, J. Chem. Phys. **109**, 2999 (1998).
[28] E. Segev and M. Shapiro, J. Chem. Phys. **77**, 5604 (1982).
[29] G. Hose and H. S. Taylor, J. Chem. Phys. **76**, 5356 (1982).
[30] R. E. Wyatt, G. Hose, and H. S. Taylor, Phys. Rev. A **28**, 815 (1983).
[31] B. Eckhardt, G. Hose, and E. Pollak, Phys. Rev. A **39**, 3776 (1989).
[32] S. Yoshida, F. Großmann, E. Persson, and J. Burgdörfer, Phys. Rev. A **69**, 043410 (2004).
[33] S. X. Sun and W. H. Miller, J. Chem. Phys. **117**, 5522 (2002).